RESEARCH ARTICLE

NANO · MICRO small
www.small-journal.com

Unraveling Exchange Coupling in Ferrites Nano-Heterostructures

Pierfrancesco Maltoni, Gianni Barucca, Bogdan Rutkowski, Maria Chiara Spadaro, Petra E. Jönsson, Gaspare Varvaro, Nader Yaacoub, José A. De Toro, Davide Peddis,* and Roland Mathieu**

The magnetic coupling of a set of $SrFe_{12}O_{19}/CoFe_2O_4$ nanocomposites is investigated. Advanced electron microscopy evidences the structural coherence and texture at the interfaces of the nanostructures. The fraction of the lower anisotropy phase ($CoFe_2O_4$) is tuned to assess the limits that define magnetically exchange-coupled interfaces by performing magnetic remanence, first-order reversal curves (FORCs), and relaxation measurements. By combining these magnetometry techniques and the structural and morphological information from X-ray diffraction, electron microscopy, and Mössbauer spectrometry, the exchange intergranular interaction is evidenced, and the critical thickness within which coupled interfaces have a uniform reversal unraveled.

1. Introduction

Magnetic interactions play a crucial role in the effectiveness of magnetic nanomaterials in industrial applications, such as magnetic recording, permanent magnets, and spintronics.[1–5] Functional oxide nanocomposites (NCs) have demonstrated great potential in this regard, based on the combination of two or more phases to create functional materials with tunable magnetic properties.[6–10] In this context, multiphase nano-heterostructures have attracted a huge interest in developing a new class of materials with enhanced magnetic properties.[11–13] In particular, the idea of maximizing the energy product of permanent magnets through the design of exchange-coupled systems made of magnetically softer (with high saturation) and harder (with large coercivity and remanent magnetization) nanocrystallites is well-established.[7,14–16] Yet, achieving an optimal exchange-coupling at the composite interfaces remains a highly debated topic, despite numerous experimental studies.[17–21] In fact, to tune the magnetic properties via magnetic interactions at the interface, many factors need careful consideration, including the size and shape of the components and, crucially, interphase details, as they affect the energy barrier distribution and, thus, the magnetization reversal. Examples of heterostructures with efficient interface exchange-coupling have mainly been reported

P. Maltoni, R. Mathieu
Department of Materials Science and Engineering
Uppsala University
Box 35, Uppsala 751 03, Sweden
E-mail: pierfrancesco.maltoni@angstrom.uu.se; roland.mathieu@angstrom.uu.se

G. Barucca, M. C. Spadaro
Dipartimento di Scienze e Ingegneria della Materia dell'Ambiente ed Urbanistica–SIMAU
Università Politecnica delle Marche
Ancona 60131, Italy

B. Rutkowski
Faculty of Metals Engineering and Industrial Computer Science
AGH University of Science and Technology
Al. A. Mickiewicza 30, Kraków 30-059, Poland

P. E. Jönsson
Department of Physics and Astronomy
Uppsala University
Box 516, Uppsala SE-751 20, Sweden

G. Varvaro, D. Peddis
Istituto di Struttura della Materia, nM^2-lab
Consiglio Nazionale delle Ricerche
Monterotondo Scalo, Rome 00015, Italy
E-mail: davide.peddis@unige.it

N. Yaacoub
Institut des Molécules et Matériaux du Mans, CNRS UMR-6283
Le Mans Université
Le Mans F-72085, France

J. A. De Toro
Instituto Regional de Investigación Científica Aplicada (IRICA) and Departamento de Física Aplicada
Universidad de Castilla-La Mancha
Ciudad Real 13071, Spain

D. Peddis
Dipartimento di Chimica e Chimica Industriale & INSTM, nM2-Lab
Università degli Studi di Genova
Via Dodecaneso 31, Genova 1-16146, Italy

The ORCID identification number(s) for the author(s) of this article can be found under https://doi.org/10.1002/smll.202304152

DOI: 10.1002/smll.202304152

in core-shell nanoparticles.[22–24] Recently, a strong coupling has also been demonstrated in more complex morphologies such as nanocomposites.[20,25–28] Such nano-heterostructures represent a challenge in the elucidation of the interface magnetic interactions. What is lacking is a proper and systematic study of the magnetic interaction in such systems. There is also the need to explore and find new material combinations to use as components in these systems, leading to optimized magnetic properties and suitable energy products, and operating temperatures.

In the present study, a series of ferrites-based NCs consisting of a hard $SrFe_{12}O_{19}$ (SFO) phase exchange-coupled with a softer $CoFe_2O_4$ (CFO) ferrite were selected to study the effect of the addition of a phase with lower anisotropy on the overall reversal process. The NCs exhibit an epitaxial growth at the interface between SFO/CFO, as a result of the controlled annealing, evidenced here by an advanced electron microscopy study. In these ferrimagnetically ordered ferrites, the indirect exchange (typically mediated by an oxygen anion between magnetic iron/cobalt cations located in each of the two coupled phases) can only take place if a coherent crystalline growth can be achieved. While the shape of the field-dependent magnetization may reflect the strong coupling between two magnetic phases, further studies are necessary to determine whether the observed coupling stems from exchange interactions.

We will demonstrate that the strong magnetic coupling has its origin in this morphology, yielding single-phase-like hysteresis loops for the composites, in contrast with inhomogeneous coarse mixtures lacking exchange coupling between the two magnetic phases. Beyond recording the isothermal magnetization as a function of the applied field (i.e., hysteresis loops), there are a number of different techniques to characterize more detail of the magnetization reversal. These include remanence plots, first-order reversal curves (FORCs) diagrams, and time-dependent (i.e., relaxation) magnetization measurements.[23] The right panels of Figure S1 (Supporting Information) illustrate the remarkable correlation between the results of these three protocols, hereby suggesting their synergetic use to be described in detail in this article.

To the best of our knowledge, for the first time, these techniques were combined to thoroughly investigate the magnetization reversal in an attempt to disentangle the aforementioned complexity and extract qualitative and quantitative information about the reversal in these nanocomposites. Our results unambiguously reveal exchange intergranular interactions and allowed us to quantify the size limit for strong magnetic coupling at the interface between interacting grains, and related to the epitaxial growth that is found to take place at the interfaces.

2. Results and Discussion

2.1. Overview of Morphological and Magnetic Properties

A series of nanocomposites comprising hexagonal-$SrFe_{12}O_{19}$/spinel-$CoFe_2O_4$ (SFO/CFO) was synthesized through one-pot sol-gel self-combustion method, using citric acid as a chelating agent.[29] Two different compositions, namely 90/10 and 50/50 SFO/CFO wt% (denoted NC_1 and NC_5, respectively), were prepared to explore the effect of CFO as nucleation site for the subsequent formation of SFO by high-temperature annealing, and the effect on the magnetic coupling between the two components. This method was chosen to synthesize homogeneously dispersed SFO and CFO particles in the submicrometric range with crystallite sizes, $\langle d \rangle^{SFO}$ and $\langle d \rangle^{CFO}$ respectively, lower than critical single-domain diameters (≈600–800 nm and ≈50 nm, respectively).[30,31] In addition, a reference sample (hereafter referred to as NC_MIX), was prepared for comparison by mechanically mixing SFO precursors and CFO (90/10 wt.%) and subsequently annealing them at the desired temperature to form the final SFO phase. The homogeneous nanocomposites are formed by crystalline platelets interconnected to form a sort of mosaic, as shown in the TEM bright field images of **Figure 1**a,b corresponding to NC_1 and NC_5 samples, respectively, and in the low magnification images of Figure S2 (Supporting Information). High-resolution (HR)TEM analysis (inset of Figure 1a) shows a well-defined texture in the growth of the two phases with the $(111)_{CFO}$ atomic planes being parallels to the $(002)_{SFO}$ ones. Moreover, the samples display a homogeneous spatial distribution of the two phases as evinced by the STEM-EDX composition maps of which an example is reported in Figure S3 (Supporting Information). STEM-EDX measurements reveal that the Co and Sr atoms are complementary in the regions where Fe and O are homogeneously distributed (Figure S3, Supporting Information), and that one phase is always associated with the presence of the other, in agreement with the HR(TEM) results where the growth of one phase on top of the other was observed. STEM-EDX is not the ideal method to quantify light elements' content and in our work, this analysis has been performed simply to visualize the oxygen spatial distribution. As expected, in NC_MIX (Figure 1c), the two magnetic phases tend to form separated agglomerates that prevent the homogeneous distribution of a phase inside the other and reduce their contact surfaces. Two regions are evidenced, which correspond to the hexagonal and cubic phases of SFO (white arrow) and CFO (green arrow), respectively, as revealed by the corresponding selected area electron diffraction (SAED) patterns (insets). In particular, the interplanar distances were calculated from the diffraction patterns and compared with those reported in the International Center for Diffraction Data (ICDD) cards for SFO (card n. 33–1340) and CFO (card n. 22–1086). The two agglomerated phases are segregated from each other; indeed, all the diffraction spots can be individually associated in one case with the single SFO phase and in the other with the single CFO phase. To further investigate the interface between SFO and CFO grains, high angular annular dark field (HAADF) STEM analysis was performed on NC_1 and NC_5 samples. A typical high-resolution HAADF-STEM image of an NC_1 interface is shown in Figure 1d. The visible contrast is due to the average atomic number of the columns of atoms in the direction of the electron beam inside the microscope (Z-contrast), therefore the experimental image is a map of the atomic positions, inside the CFO and SFO crystals, projected in the electron beam direction. The experimental image was compared with the expected distribution of atoms in the CFO and SFO phases opportunely projected, as evidenced in the atomic model included in the image. In particular, pink circles describe the position of the Co/Fe atoms inside the CFO crystal projected along the $[1\text{-}10]_{CFO}$ direction, while green and light blue circles are the position of Sr and Fe atoms, respectively, in

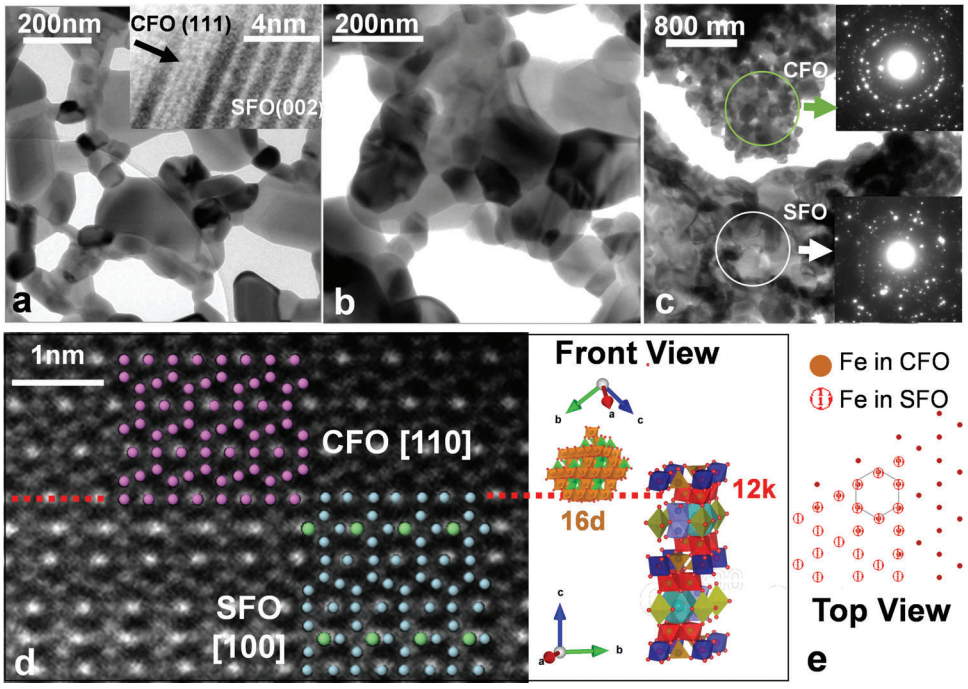

Figure 1. Bright-field TEM images showing the nanocomposites morphology: a) NC_1, b) NC_5, and c) NC_MIX. Inset of (a) shows a high-resolution (HR)TEM image revealing the oriented growth of the SFO and CFO phases in NC_1; insets of (c) are SAED patterns taken in the evidenced areas of the sample. d) High-resolution HAADF-STEM image of a typical SFO/CFO interface in NC_1 (red line): atomic models of SFO (green-Sr^{2+} and light-blue-Fe^{3+} dots) and CFO (pink dots) crystals are superimposed. e) Model showing the distribution of the atoms at the interface plane according to whether they belong to the CFO phase (dark orange dots) or to the SFO phase (red circles). "Front view" or "top view" refers to the direction in which the interface atomic plane can be observed.

the SFO crystal projected along the $[100]_{SFO}$ direction. Oxygen atoms are not visible in the experimental image (low atomic number) and are not shown in the simulated crystals either. The good agreement between the experimental atomic positions and the atomic model has allowed to identify the orientation relationships between the two phases, $(001)_{SFO}//(111)_{CFO}$ and $[100]_{SFO}//[1\text{-}10]_{CFO}$, and the atomic plane corresponding to the interface between the two phases. Similar growth directions have been detected in other structures, such as $BaFe_{15}O_{23}$/ Fe_2O_3.[21] The interface plane is perpendicular to the $[111]_{CFO}$ direction in the CFO phase and it is composed of Fe/Co atoms, belonging only to the octahedral sites of the spinel structure, which give rise to the spatial distribution shown in Figure 1e as dark orange dots. The dots are distributed in a hexagonal-like structure and the distance between the nearest neighbors is always 0.296 nm. Looking at the SFO phase, the interface plane is perpendicular to the $[001]_{SFO}$ direction and it corresponds to the plane composed of only Fe atoms belonging to the octahedral 12k position in the hexagonal SFO lattice (also Figure S4, Supporting Information). The 12k Fe atoms give rise to the spatial distribution shown in Figure 1e as red/white circles, and they have exactly the same distribution as the previous Fe/Co atoms described by dark orange dots. The only difference is the distance among nearest neighbors (equal to 0.291 nm on one side and 0.298 nm on the other; see Supporting Information for more details), being however in average 0.2945 nm, very similar to the previous one of 0.296 nm. This result indicates that the interface plane between the two phases can be perfectly shared by the CFO and SFO phases. Starting from this plane, on one side the Co/Fe atoms are distributed forming a spinel structure, while on the other side, Sr and Fe atoms are organized to form the hexagonal lattice. Consequently, this epitaxial growth gives rise to a strong magnetic coupling between the two phases. The same interfaces were typically observed in sample NC_5 indicating that this epitaxial growth is characteristic of SFO/CFO nanocomposites synthesized with the procedure reported in our previous study.[29] It is important to highlight that the same type of epitaxial growth has been observed by Belec et al. in $BaFe_{15}O_{23}$/ Fe_2O_3,[21] where composite nanoplatelets have been prepared by seed-mediated approach based on co-precipitation synthesis. It should be underlined that co-precipitation and self-combustion synthesis have completely different thermodynamic profiles, suggesting that the observed epitaxial growth is independent of the synthesis method and on the stoichiometry of the spinel phase.

To establish the role of the interface in the coupling interaction, ^{57}Fe Mössbauer spectra were recorded at room temperature (300K) and 77 K for the whole set of samples (see Figures S5–S8, Supporting Information). The obtained hyperfine parameters and spectral areas for SFO (in Tables S1 and S2, Supporting Information) are all reasonably in agreement with other reports.[32,33] The room temperature spectra for NCs are the direct result of the combination between sextets of SFO and CFO phase, whose overlapping and superposition of sub-spectra resulting from the tetrahedral and octahedral sites of both phases result in mean values for all the hyperfine parameters, except for

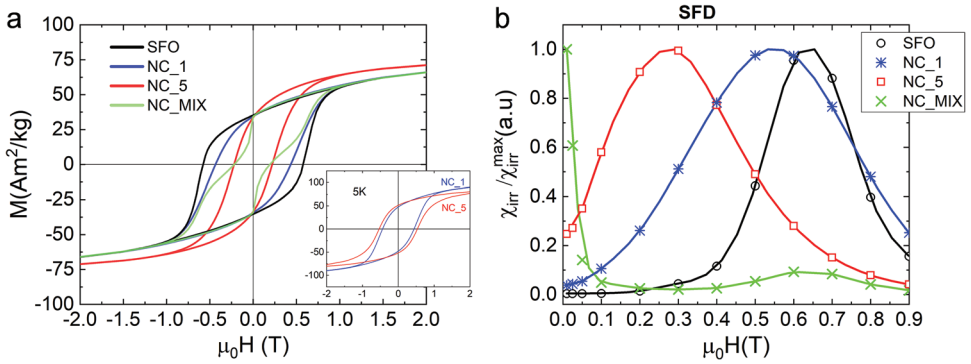

Figure 2. a) Room temperature magnetization *M* versus magnetic field *H* loops; in the inset, *M* versus *H* loops measured at 5K for NC_1 and NC_5. b) Corresponding normalized irreversible component of the susceptibility, χ_{irr}.

$12k^{SFO}$ that allow the quantification of SFO and CFO wt.% (found to match XRF analysis). They reveal the presence of an additional component (fit 4) with hyperfine field values (42.5–43.3 T) similar to $12k^{SFO}$ site in the composite, but different from octahedral sites for pure SFO and CFO, which may correspond to a different environment for the octahedral sites at the CFO-SFO interface, which are shared between the two phases. This matches the (HR)TEM analysis, and it was observed for the full set of nanocomposites.

The optimized interface along with the homogeneous distribution of particles, results in a fully-coupled magnetic response (**Figure 2**a). The composites present single-phase-like loops at room temperature with coercivities, H_C, ranging from ≈0.22 to ≈0.58T, demonstrating the absence of phase segregation, which would yield a double-loop (also known as constricted or "hummingbird") curves, owing to the difference in coercivity of the two constituent phases, shown in Figure S9 (Supporting Information).[34–37] Although such decoupling has been observed before at low temperatures in systems effectively coupled at room temperature,[38,39] the present nanocomposites do not exhibit double loops down to 5K (see the inset of Figure 2a for NC_1 and NC_5). This is a consequence of the increasing coercivity of CFO particles at 5K compared to the slightly lower coercivity of SFO at 5K, which makes the difference in magnetic anisotropy between the two phases smaller, thus making the coupling even stronger (see Figure S9, Supporting Information). Incidentally, the coercivity of NC_5 at low temperature overcomes that of NC_1.

The observed magnetic behavior of the homogeneous nanocomposites is in stark contrast with the clear double-loop *M* versus *H* curve of the NC_MIX sample, whose uncontrolled growth of both phases, due to the physical method compared to the chemical synthesis for NCs, was confirmed by X-ray powder diffraction (XRPD) analysis that shows much larger CFO crystallites than those in NC_1 (85 nm and 20 nm, respectively, see **Table 1**). On the other hand, in the one-pot synthesis each phase prevents the growth of the other, and, in turn, we expect an effective coupling in systems for which the critical thickness of the softer phase does not exceed around twice the width of the domain wall of the hard magnetic phase.[7,10] The coercive field of the nanocomposites (labeled "$\mu_0 H_C$(Exp)" in Table 1) is significantly smaller than those extracted from the calculated superposition of the constituent members (labeled "$\mu_0 H_C$(Calc)"), especially for NC_MIX sample (for info on the calculation see Section S4 and Figure S10, Supporting Information). The reduced coercivity of the NCs with respect to the simple (decoupled) superposition of the two phases is mainly due to the incorporation of a lower anisotropy phase (CFO). This i) reduces the coercivity of the SFO phase as expected by the corresponding reduction of crystallite size of SFO achieved by one-pot synthesis (from 118 down to 64 nm when introducing 50 wt.% of CFO)[30,40]; and ii) may promote incoherent or even multi-domain reversal modes (the critical diameter for single domain Co ferrites has been established to be between 40 nm and 70 nm).[31,41,42]

The latter seems also to be the case for NC_MIX, whose CFO crystallite size is equal to 85 nm as a consequence of the segregation (as confirmed by TEM, see Figure 1c), where, despite the rather close composition to NC_1, the coercive field drops to 0.2 T. Furthermore, the analysis performed by XRF hints at the presence of an additional Fe rich phase in this sample (see Table 1); given the high annealing temperature, we may not exclude the presence of antiferromagnetic hematite, or spinel maghemite, as recently shown by P. Shyam et al.,[35] owing to an incomplete formation of the hexagonal phase during the annealing (which agrees reasonably well with the observed slight increase of the saturation magnetization, M_S, with respect to NC_1), at the expense of the SFO content.

The coupled/decoupled magnetic response was studied in depth by investigating the irreversible process of

Table 1. Overview of the crystallites size of SFO ($\langle d\rangle^{SFO}$) and CFO ($\langle d\rangle^{CFO}$) in the NCs,[29] and NC_MIX extracted from XRPD, and compositions by XRF. Experimental ($\mu_0 H_C$(Exp)) and calculated ($\mu_0 H_C$(Calc)) coercive fields as a function of $\frac{\langle d\rangle^{SFO}}{\langle d\rangle^{CFO}}$ (uncertainties are reported between brackets).

Id	$\langle d\rangle^{SFO}$ [nm]	$\langle d\rangle^{CFO}$ [nm]	SFO/CFO wt%	$\frac{\langle d\rangle^{SFO}}{\langle d\rangle^{CFO}}$	$\mu_0 H_C$[Exp] [T]	$\mu_0 H_C$[Calc] [T]
SFO	118(5)	–	Reference[a)]	–	0.58(3)	–
NC_1	93(4)	20(2)	89/11(1)	4.6	0.43(2)	0.54(2)
NC_5	64(9)	65(2)	51/49 (2)	0.9	0.22(1)	0.34(2)
NC_MIX	119(10)	85(8)	88/10/2[b)] (2)	1.4	0.20(1)	0.50(4)

[a)] assumed stoichiometrically correct by ICP-analysis and used as a standard for the composite measurements (100%); [b)] Fe-rich phase excess.

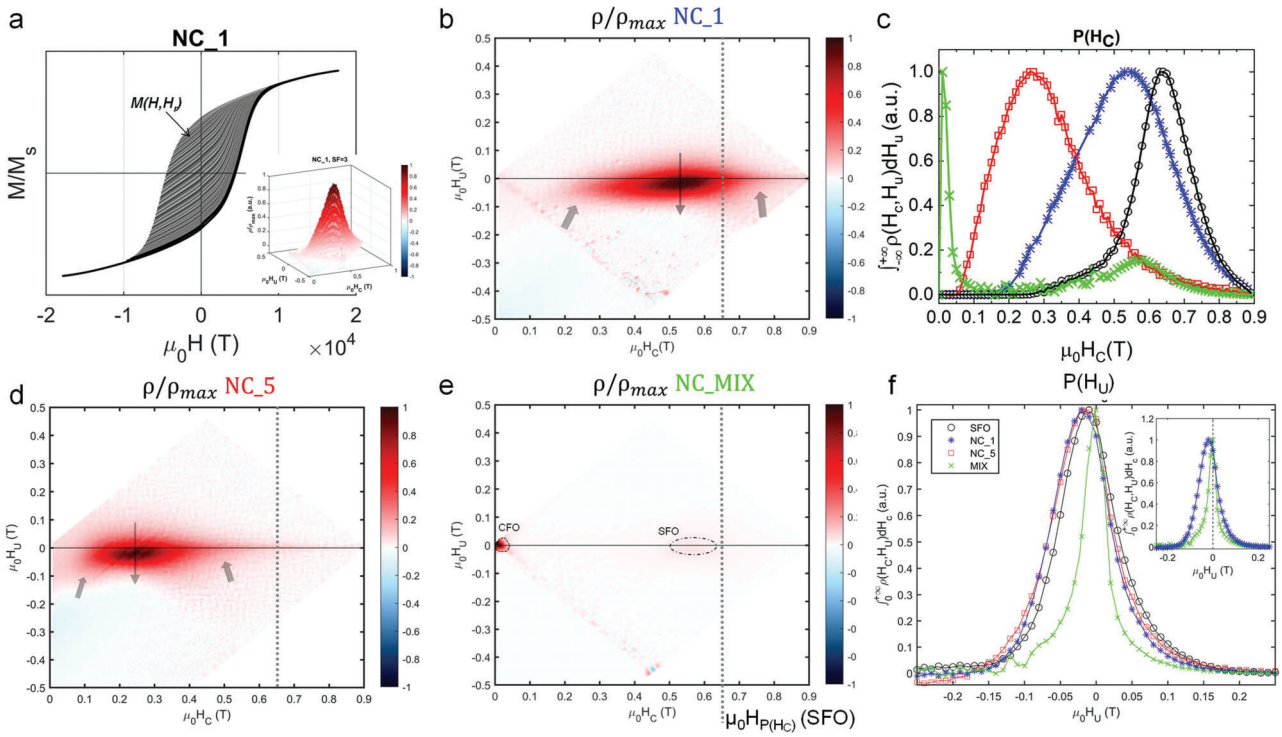

Figure 3. a) FORCs used to determine the mixed partial derivative $\rho(H, H_r)$ shown in the inset; c) corresponding projection $P(H_C)$ along the coercivity, H_C. b,d,e) FORCs diagrams as a function of H_C and H_U for NC_1, NC_MIX, and NC_5, respectively. f) FORCs projections along H_U axis. The thick and thin arrows in (b,d) indicate the downward shift and additional side humps, respectively. The dashed regions in (e) show the CFO and SFO independent switching. The vertical dotted lines in (b, d, e) mark H_C^{SFO}.

magnetization reversal through the analysis of the DCD curves (shown in Figure S11, Supporting Information).[23] The first derivative of the curve with respect to the magnetic field corresponds to the irreversible susceptibility $\chi_{irr}(H)$, which represents a measure of the energy barrier distribution (associated with the particles switching field distribution, SFD). The SFDs obtained for the nanocomposites show a uniform reversal, while that for NC_MIX clearly reveals two contributions centered at fields that can be attributed to the reversal processes of the two individual phases (SFO and CFO), Figure 2b. For comparison, we prepared two physically mixed samples with preformed particles without any heat treatment, thereby having SFO and CFO crystallite sizes of the same order as in NC_1 (see Figure S12, Supporting Information). Surprisingly, SFDs show that, as the particles are closer in contact, the response becomes more single-peaked, and no shift toward switching fields, H_{SW}, smaller than SFO's is observed. Since the particles do not share clear interfaces (they are not "intergrown"), such interactions must be exclusively of dipolar nature. This evidence reinforces our claim for NC_MIX to be a decoupled system.

2.2. First-Order Reversal Curves (FORCs) Results

A uniform (single-peaked) response in the SFD is usually taken as evidence of a collective reversal process, however, it may hide certain features produced by both long-range dipolar and short-range exchange interactions between the particles. In this context First-Order Reversal Curves (FORCs) measurements, such as that shown in **Figure 3**a (see Experimental Section for description) enable a more accurate determination of the coercive field distribution, as well as the magnetic interactions in a multiphase nanosystem.[43–45] The high accuracy is gained at the expense of a long measurement time, with ≈500 times more data points than a single hysteresis loop, which permits to distinguish the fingerprints of different types of magnetic contributions in multiphase systems.

Figure 3b,d,e) left column shows a selection of FORCs diagrams extracted from the analysis of FORCs. We observe a single intense ridge in NC_1 evidencing a strongly coupled system, which behaves as a rigid magnet in which the two phases reverse collectively.[46] The integrated component along H_U, $P(H_C)$ projection in (Figure 3c), reveals a continuous evolution of the response toward smaller H_C from SFO to NC_5, upon increasing the CFO fraction. Noticeably, a wider $P(H_C)$ distribution for NC_1 and NC_5 can be appreciated compared to SFO (see Figure S13, Supporting Information), as it represents the distribution of coupling strengths between heterogeneous crystallites (size distribution) across interfaces (with a likely distribution of epitaxial quality) that possibly causes the wide distribution in H_C. In other words, such distributions should be analogous to the SFDs extracted from M_{DCD}, and qualitatively they do follow the same trend.

The less intense tails, or side humps, with different slopes departing from the "core" maximum along H_U in the FORCs diagrams (grey arrows) are considered fingerprints of more complex reversal mechanisms due to interparticle dipolar coupling (i.e.,

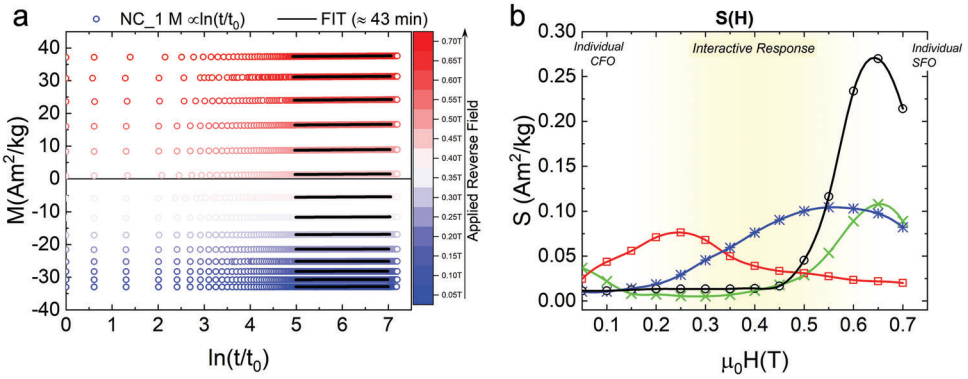

Figure 4. a) Relaxation curves, $M(t)$, of NC_1 for several positive reversal fields; b) magnetic viscosity $S(H) = \frac{dM}{dln(t)}$ of the selected samples at 300K, estimated by fitting the $M(t)$ for each reversal field.

demagnetizing effects) and thermal relaxation.[47,48] A closer look at the maps confirms the magnetizing nature of the interactions (i.e., the exchange coupling), as the low-H_C sector is shifted in the negative H_U direction and accompanied by a curvature in the lower half of the contour plots.[49] Integrating along H_C gives the vertical projections $P(H_U)$ shown in Figure 3f, which confirm the shift to negative H_U values for the full set of samples except for NC_MIX, where the lack of such bias (as better observed in the inset of Figure 3f) and the narrow H_U distribution indicate that most of the particles are not exchange-coupled, as expected in this sample. Indeed, the diagram (Figure 3e) exhibits two modes centered at low $\mu_0 H_C$ and at $\mu_0 H_C = \mu_0 H_C{}^{SFO} \approx 0.65$T, revealing the individual switching of the two phases (i.e., a decoupled system), rather than a continuous distribution. The tight distribution of contours along the H_U axis reflects the non-interacting nature of the magnetic CFO particles (see Section S6.2, Supporting Information for additional comments). This is consistent with the nature of the synthetic method employed to purposefully prepare a decoupled composite, confirming the separation between the two systems. The $P(H_U)$ projections were fitted to different functions in an attempt to discriminate between different magnetic interactions (see Figures S14 and S15, Supporting Information),[48] strengthening the results previously discussed.

Additionally, for a certain combination of hard and soft phases, we expect to observe rigid coupling only up to a critical thickness of the softer phase. According to the Goto model for interfacial exchange-spring coupling the maximum thickness of the softer phase through which the rigid coupling can extend is called the critical thickness,[12,50] given by $d_{crit}^{soft} = \sqrt{\frac{\pi^2 A^{soft}}{2 M_S^{soft} \mu_0 H_r^{hard}}}$ where A^{soft} and $M_S{}^{soft}$ are the exchange stiffness and saturation magnetization of the softer phase, respectively, and $H_r{}^{hard}$ is the reversal field of the hard phase. Considering the experimental values in this work (and calculating the uncertainty by replacing them with the standard values for CFO and SFO) a large critical thickness of 20 (5) nm was found, as expected, from the moderate magnetocrystalline anisotropy contrast between the two phases $K_1{}^{SFO}/K_1{}^{CFO} \cong 1.2$.[31] This translates into small differences in the individual switching of the components, and thus the full coupling is not prevented for larger distances.

FORCs measurements thus provide direct evidence of strong exchange coupling in these samples. Nonetheless, we will show that the wide distribution of coercivities $P(H_C)$ obtained for NC_1 and NC_5 cannot be fitted by a single peak function, suggesting a more complex reversal process possibly involving several overlapped, which could appear on different timescales due to the different coupling regime determined by the content of SFO and CFO in the composites.

2.3. Relaxation M(*t*) Measurements

From magnetic relaxation measurements (shown for NC_1 as an example in **Figure 4**a), it is possible to determine the magnetic viscosity, $dM/dln(t)$, which describes the thermally activated transition over an energy barrier.[51] It is field-dependent and normally is highest close to the coercive field, reflecting the connection between $S(H)$ and $\chi_{irr}(H)$, as both are ultimately determined by the system's energy barrier distribution. The $S(H)$ curves are plotted in Figure 4b.

They reproduce closely the previous SFDs and $P(H_C)$ projections for all samples. As expected, the thermal-activated transition of NC_5 over the energy barrier appears at lower fields than that of NC_1, while NC_MIX shows two separate viscosity modes, with a perfect agreement between the independent SFO component and the corresponding H_{SW} (see Figure S16, Supporting Information for more details). The $S(H)$ curve of the NCs seems to comprise several contributions akin to the FORCs-determined $P(H_C)$ curves depicted in Figure 3b. A cumulative fitting of $S(H)$ with Gaussian-like functions was performed as illustrated in **Figure 5**a,c for NC_1 and NC_5. Up to three contributions were identified, and ascribed to three different reversal modes, corresponding to different regions of the particles: generally, the end modes of SFO and CFO, respectively appearing at higher and lower switching fields, and the strongly coupled interface (red curve). As shown in Figure 5b,d, the results agree remarkably well with those obtained from the fitting of the $P(H_C)$ projections from FORCs, which display the same number of reversal components.

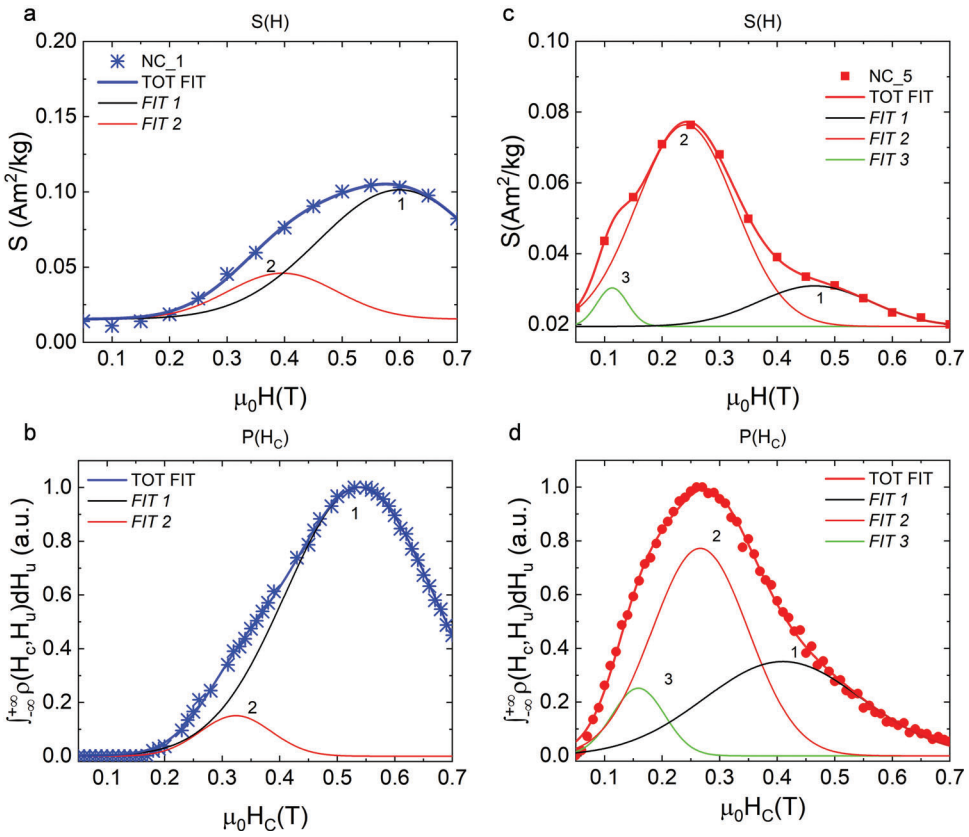

Figure 5. a) Example of fitting of *S(H)* for NC_1; b) fitting of the FORCs' distribution along H_C; (c,d) show the corresponding results for NC_5.

Next, the activation volume, V_{ACT} defined as the volume involved in the process of overcoming the energy barrier for magnetization reversal, was derived, aiming at clarifying the reversal magnetization process, by considering its correlation with magnetic interactions.[52,53] The values of the corresponding coherent sizes d_{coh} (effective diameter of the activation volume) are reported in Table 2.

Considering NC_1, with a small CFO fraction (10 wt.%), the CFO crystallite size ($<d>^{CFO}$ = 20 nm) matches $\mathbf{d}_{crit}^{soft}$ defined above, supporting our claim of a rigidly coupled system. If the nanocrystallites are strongly exchanged-coupled, this should yield an activation volume comprising a significant number of nanocrystallites.[54–59] Indeed, as displayed in **Table 2**, the calculated coherent size for component (2), $d_{coh,2}$, is ≈40 nm, twice the size of the CFO grains, and therefore the corresponding activation volume $V_{(act,2)} \approx 2^3 <V>^{CFO}$, i.e., about an order of magnitude larger than the average CFO crystallite volume extracted from XRPD.

Interestingly, $d_{coh,2}$ is constant across the series of NCs (**Figure 6**a), which implies, assuming the same critical thickness $\mathbf{d}_{crit}^{soft}$, that the corresponding rigidly coupled area is maintained invariant for all the investigated composites despite the addition of a larger fraction of the CFO phase. This supports our hypothesis that the second, most intense, reversal component in the fits corresponds to the reversal of SFO/CFO crystallites strongly coupled at their interface, with the two phases' magnetization reversing coherently as a single component.[7,21] Thus, when we increase the CFO fraction up to 30 wt.% (i.e., additional NC_3 sample, see Figure S18, Supporting Information) and then 50 wt.%, this rigid coupling does not extend to the whole phase, as in these samples the CFO size $<d>^{CFO}$ increases up to 65 nm. In this scenario, we also observe individual-like reversal modes for CFO (component 3) and SFO (component 1) in regions far from the interface. Interestingly, $d_{coh,1}$ (corresponding to the individual SFO reversal) increases across the series by 64% (Figure 6a), suggesting that the interaction volume of that component is enhanced by the higher number of SFO/CFO interfaces affecting the reversal in the

Table 2. Crystallite size (*<d>*, from XRPD) versus magnetic size (d_{coh}, from magnetic viscosity measurements).

Id	Crystallites Size		Coherent Size [From high reverse field to low]		
	$<d>^{SFO}$ [nm]	$<d>^{CFO}$ [nm]	$d_{coh,1}$ [nm]	$d_{coh,2}$ [nm]	$d_{coh,3}$ [nm]
SFO	118(5)[a)]	–	28(4)	–	–
NC_1	93(4)	20(2)	29(1)	39(3)	–
NC_3	68(5)	48(3)	41(5)	38(3)	39(5)
NC_5	64(9)	65(2)	46(8)	38(3)	48(7)
NC_MIX	119(10)	85(8)	27(1)	–	32(8)

[a)] Uncertainties were calculated according to the choice of background in the fitting, see Figure S17 (Supporting Information).

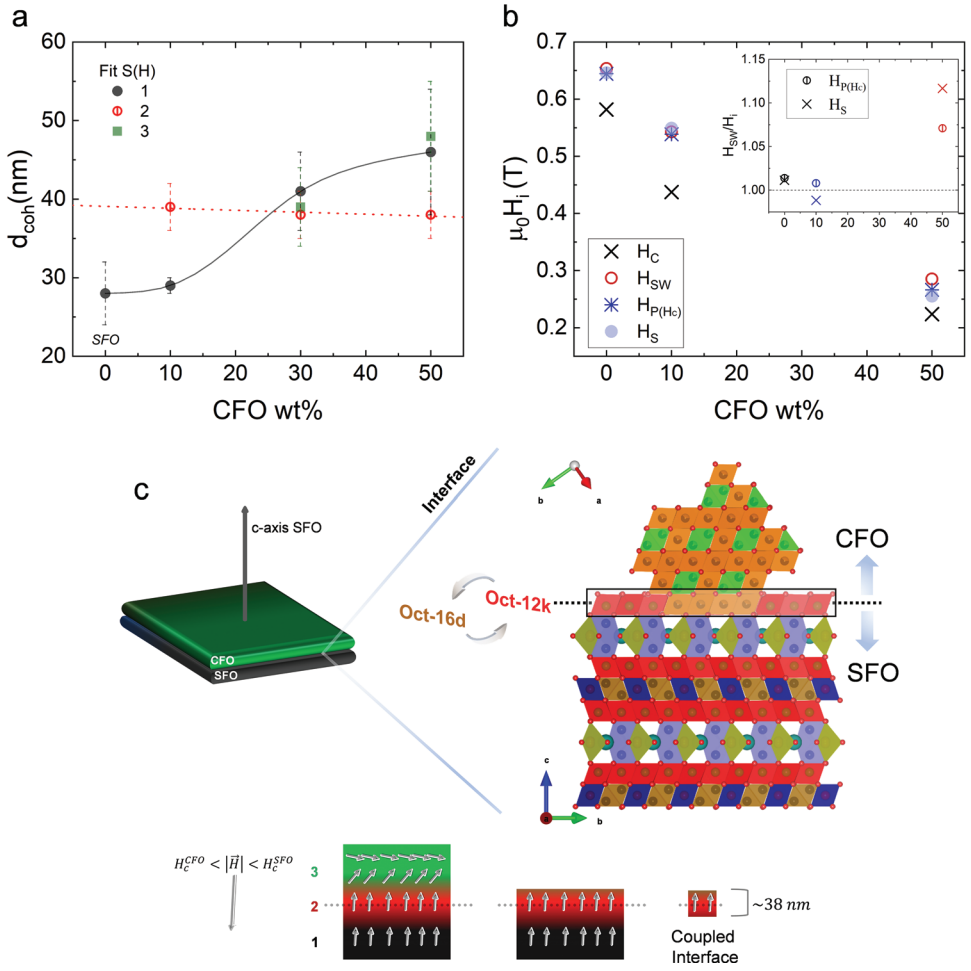

Figure 6. a) Coherent sizes d_{coh} (indices 1-2-3 refer to magnetic components extracted from the fitting); the red dashed line is a linear fitting (with a nearly zero slope) for the critical thickness of the CFO phase. b) Summary of all the field parameters H_C, H_{SW}, H_S, $H_{(P(Hc))}$, from the experimental measurements. In the inset, ratios between H_{SW} (from SFD) and H:H_S (from viscosity) and $H_{(P(Hc))}$, (from FORC projections along H_C) are shown; c) SFO/CFO interface with the crystallographic orientation, and sketch of the magnetic reversal mechanism when the CFO fraction increases.

composite. This description corresponds to a "spring magnet", since the addition of a softer phase causes the reduction/increase of the SFO/CFO coherent reversal sizes and, concomitantly, the reversal process for each phase becomes less hard/soft. The same trend could be observed for the CFO fraction. On the other hand, in NC_MIX two clearly well-separated components were found, respectively at high fields for SFO and low field for CFO: the coherent diameter was estimated, and found to agree with data obtained for CFO particles reversing independently (Figure S19, Supporting Information).

The observed increase of activation volume for the coupled regions can be explained by the intergranular exchange interaction acting exclusively between nanocrystallites of SFO and CFO that are in direct contact. In the more complex NCs with higher CFO fractions with grain sizes above the critical thickness, only a restricted interface softer region pinned by the hard phase reverses with it, revealing exchange-spring phenomena. In Figure 6b a summary of the different field parameters is presented, highlighting the remarkable agreement. In fact, the inset reveals that the ratios between the switching field from DCD and the field parameters extracted by viscosity and FORCs projection (H_{SW}/H_S and $H_{SW}/H_{P(Hc)}$, respectively) are ≈1 for SFO and NC_1 as expected for systems in the absence of reversible processes, while for NC_5 the value deviates from 1, hinting at a more complex reversal process.

Our nano-heterostructures are the result of the high control of interface epitaxy achieved through controlled annealing, which produces a [100]//[1–10] texture between SFO and CFO induced by the (111) of preformed CFO (as depicted in Figure 6c, together with a schematic of the reversal). Knowing that the easy axes are not parallel to each other (while the SFO core has an out-of-plane easy axis, the CFO layer tends to lie along the [100] axis)[60,61] induce to believe that the strong coupling is not due to dipolar interaction between the two materials, as it may be the case for such misinterpretation if the easy axes were aligned. In contrast, the physically mixed systems (with similar size as in NC_1) for which we do not expect any exchange-coupling, show an agreement with the superposition of the members, even when the two phases are in closer contact (by applying pressure) thus expecting higher dipolar interactions (as previously shown

in Figure S12, Supporting Information). This comparison suggests an interesting alternative to combine two magnetic phases, by obtaining a compromise between the size of the phase with lower anisotropy and different types of particle interactions.[39] The potential as permanent magnets of nanocomposites, based on exchange-coupled $SrFe_{12}O_{19}/CoFe_2O_4$ nanocrystallites, was evaluated by compacting the nanostructured powders into disc-like pellets via spark plasma sintering (SPS) and measuring their out-of-plane (oop) hysteresis loop in order to evaluate the energy product. The details will be discussed in a separate study. The resulting high-density magnet prepared from NC_1 (with a packing fraction of 90% relative to the bulk), labeled SPS_NC_1, is shown in Figure S21 (Supporting Information): it exhibits a square-like shape, with a notable increase of the remanent magnetization compared to the nanopowders. The experimental $(BH)_{MAX}$ ≈16 kJ m^{-3} shows a remarkable increase of ≈45% compared to that of the SFO phase.

3. Conclusion

The epitaxial growth and local texture at the interfaces of SFO/CFO nanocomposites were evidenced by electron microscopy. We have illustrated the correlations between several magnetic protocols of different complexity to tackle the role of interactions in multiphase systems. The synergetic combination of FORCs and relaxation measurements helps to get a deeper understanding of the different mechanisms at play between ferrimagnetic particles with different magnetic anisotropy, not only qualitatively but also quantitatively. FORCs suggest a strong intergranular exchange coupling. The magnetic coherence length scales were estimated and compared to the critical soft thickness, in order to establish the limit of the rigid coupling regime in this kind of ferrites. Finally, our results corroborate a number of experimental studies,[21,35,39,62] indicating that the quick deterioration of the hard phase properties typically observed upon the introduction of a phase with lower anisotropy in nanocomposites may be avoided by developing synthesis conditions that allow to control and reduce the size of the lower anisotropy phase, engineer the interfaces to avoid impurities, and thus tailor the magnetic properties.

4. Experimental Section

Samples Details: Two sets of samples were prepared:

1) A series comprising the individual pure $SrFe_{12}O_{19}$ (SFO) and two nanocomposites with different weight fraction wt.% of $CoFe_2O_4$ (CFO): NC_1 and NC_5 (10 and 50 wt.% CFO, respectively). Briefly, the composites were prepared by a sol-gel synthesis using Fe, Sr, and Co nitrates in an appropriate ratio, and citric acid as chelating agent; the post-synthesis powder-like products were subsequently annealed at 950 °C for 3 h with a ramp of 5 °C min^{-1} under air.[29] All the samples are composed of interconnected particles (see Figure 2). The increasing CFO fraction in the composite prevents the grain growth of SFO, resulting in a decrease of the average SFO crystallites size from 118 down to 64 nm in NC_5 (≈45% reduction), and vice-versa for CFO (an increase from 20 to 65 nm). The density of the samples was assumed to be ≈30% of the bulk one (5290 kg m^{-3} for CFO and 5100 kg m^{-3} for SFO).[29]
2) A series of assemblies prepared by physically mixing CFO-particles (≈20 nm in size, obtained by sol-gel self-combustion) and the precursors of SFO (products of post-combustion from sol-gel, i.e., $SrCO_3$, and Fe-oxides) in a mortar for 1 h to obtain the desired final wt.% of 90/10 SFO/CFO, which were then annealed to form the hexagonal SFO phase (referred as NC_MIX). The uncontrolled and segregated growth of both phases (Figure 2c) does not favor the exchange coupling of the two phases, as shown in this study. For comparison, to investigate the role of magnetic interactions in more detail, two additional systems were prepared for reference: i) NMIX, by mixing the same CFO-particles ($\langle d \rangle^{CFO}$ ≈20 nm) with the preformed SFO ones from point (1) above without further treatments; and ii) NMIX-P, by pressing NMIX with an applied pressure of a ≈$6.3 \cdot 10^2$ MPa.

Characterization: Transmission electron microscopy (TEM) studies were carried out in a Philips CM200 microscope operating at 200 kV and equipped with a LaB_6 filament. Scanning-transmission electron microscopy (STEM) analysis was carried out with a probe Cs-corrected FEI Titan3 G2 60–300 STEM equipped with ChemiSTEM technology (X-FEG field emission gun and Super-X EDX detector system) developed at FEI (FEI application note AN002707-2010) for energy dispersive X-ray (EDX) microanalysis. Samples for TEM and STEM observations were prepared by dispersing a small amount of the sample, in the form of a powder, in ethylic alcohol, and the solution was submitted to ultrasonic agitation for 1 min. A drop of the suspension was then deposited on a commercial TEM grid covered with a holed thin carbon film, and the grid was kept in the air until complete ethanol evaporation. The atomic models of the SFO and CFO phases were created by using Rhodius software from Universidad de Cadiz (Pérez-Omil, J.A. TEM-UCA software (2018). University of Cádiz. http://www.uca.es/tem-uca).[63]

The powder samples were characterized by using a Bruker D8 Advance diffractometer (solid state rapid LynxEye detector, Cu Kα radiation, Bragg–Brentano geometry, DIFFRACT plus software) in the 10°–140° 2θ range with a step size of 0.013° (counting time was 4 s per step). The powder samples were grounded in an agate mortar and suspended in ethanol. A Si substrate was covered with several drops of the resulting suspension, leaving randomly oriented crystallites after drying. Rietveld analysis was performed on the X-ray powder diffraction (XRPD) data by using the FULLPROF program (see SI for more details on the refinement).[64] The diffraction peaks were described by a modified Thompson–Cox–Hastings pseudo-Voigt function. A peak asymmetry correction was made for angles below 40°(2θ). Background intensities were estimated by interpolating between up to 60 selected points. In the Rietveld model, the CFO was described assuming a Co:Fe stoichiometry of 1:2 and a random cationic distribution between the crystallographic sites (equivalent). A NIST LaB_6 660b standard was measured under the same conditions as the samples to account for the instrumental contribution to the peak broadening. The volume-weighted average crystallite size for SFO (space group $P6_3/mmc$) was refined as anisotropic platelets.[65] For the CFO (Fd-3m) phase, it was calculated by assuming isotropic crystallites and thus using the Scherrer formula: $d_{hkl} = (K\lambda)/(\beta \cos\theta)$ where d_{hkl} is the average volume-weighted crystallite size, λ is the wavelength, θ is the scattering angle, β is the integral breadth and K is the Scherrer shape factor (assumed to be 0.9 for spherical particles).[66]

Elemental analysis was performed by X-ray fluorescence (XRF) on the selected samples, showing that only slight deviations from the target composition were observed (±2 wt.%). SFO and CFO powder samples were adopted as standards for the analysis, by checking their atomic composition (Fe/Sr:12 and Fe/Co:2) by inductively coupled plasma optical emission spectroscopy (ICP-OES).

^{57}Fe Mössbauer spectra were recorded using a ^{57}Co/Rh γ-ray source mounted on an electromagnetic transducer with velocity modulated according to a triangular waveform. The spectra were obtained at 300 and 77 K without an external applied field. The hyperfine structure was modeled by means of a least-square fitting procedure involving Zeeman sextets composed of Lorentzian lines. The isomer shift (IS) values were referred to that of α-Fe at 300 K.

Isothermal field-dependent magnetization loops were recorded at 300 and 5K (using a Quantum Design MPMS SQUID magnetometer), by sweeping the field in the −5T to +5T range, and the obtained magnetization values were normalized by the weight of powders present in the sample and expressed in $Am^2\ kg^{-1}$. To get information about the irreversible processes, direct current demagnetization (DCD) remanence curves were measured by applying a progressively higher DC reverse field to a sample previously saturated under a field of −5T and by recording, for each step, the value of the remanent magnetization, which was then plotted as a function of the reverse field. Magnetization reversal characteristics of the samples were studied using two different techniques: i) FORCs method and ii) relaxation measurements.[67,68] i) FORCs were recorded at 300K using a vibrating sample magnetometer (VSM; Lake Shore VSM model 7400) operated in a field range of ±2 T. A strong magnetic field was applied to first saturate the sample. The field was then lowered to a specified reversal field H_r, and the magnetization was measured as H was increased back to saturation. A series of these measurements at various reversal fields made up a complete set of FORCs. The FORC distribution was then determined using a mixed partial derivative $\rho(H,H_r)$, calculated using the FORCinel algorithm implemented in a Matlab code,[69,70] and then expressed in terms of the local coercivity $\boldsymbol{H_C} = (\boldsymbol{H} - \boldsymbol{H_r})/2$ and bias field $\boldsymbol{H_U} = (\boldsymbol{H} + \boldsymbol{H_r})/2$.[68] Integration of $\rho(H,H_r)$ along H_U and H_C leads to the projection of the FORC distribution $P(H_C) = \int_{-\infty}^{+\infty} \rho(H_C, H_U)\, dH_U)$ and $P(H_U) = \int_0^{+\infty} \rho(H_C, H_U)\, dH_C)$ axes, respectively. ii) Magnetic relaxation measurements were performed at 300K by two different instruments: a physical property measurement system (PPMS)-Vibrating Sample magnetometer (VSM) from Quantum Design, equipped with a superconducting magnet of 9T, and repeated on the same samples by a MicroSense Model 10 VSM equipped with an electromagnet generating a maximum field of 2T, to rule out possible effects caused by different sweeping ratios when the field was applied (see Supporting Information for details on reproducibility). The magnetization at 300K was recorded for 60 min in a reverse field after saturation in a given direction. The so-called magnetic viscosity (S) was estimated for each applied field considering $M(t) \propto S \ln(t)$.

Supporting Information

Supporting Information is available from the Wiley Online Library or from the author.

Acknowledgements

This work was supported by the Swedish Energy Agency (project number 46561-1), the Swedish Research Council (VR), the Junta de Castilla-La Mancha (SBPLY/21/180501/000226) and has received funding from the European Union's Horizon 2020 research and innovation program under grant agreement no. 823717–ESTEEM3 (Enabling Science and Technology through European Electron Microscopy). P.M. also thanks K G Westmans stipendiestiftelse. P.M., D.P., and G.V. thank Dr. César de Julián Fernández for helpful discussions.

Conflict of Interest

The authors declare no conflict of interest.

Author Contributions

The paper and Supporting Information were written based on the contributions of all authors. R.M. and D.P. designed the experiments; they coordinated the data analysis and discussion. P.M. synthesized the nanocomposites, and characterized them by XRPD, XRF, and magnetometry techniques. P.E.J. supported P.M. in the FORCs analysis. P.M., G.V., and D.P. coordinated the relaxation measurements. G.B., M.C.S., and B.R. characterized the systems and analyzed the data by HRTEM, STEM-HAAD, and EELS. N.Y. performed Mössbauer spectroscopy. R.M., D.P., and J.A.D.T. coordinated the discussion on magnetism. All authors contributed to the results, discussion, and revision of the article, which was written mainly by P.M. and R.M.

Data Availability Statement

The data that support the findings of this study are available from the corresponding author upon reasonable request.

Keywords

exchange-coupling, ferrites, interfaces, magnetic composites, permanent magnets

Received: May 17, 2023
Revised: October 10, 2023
Published online:

[1] J. U. Thiele, S. Maat, E. E. Fullerton, *Appl. Phys. Lett.* **2003**, *82*, 2859.
[2] E. Lottini, A. López-Ortega, G. Bertoni, S. Turner, M. Meledina, G. Van Tendeloo, C. De Julián Fernández, C. Sangregorio, *Chem. Mater.* **2016**, *28*, 4214.
[3] L.-C. Yu, Y.-L. Lai, M.-W. Lin, H.-W. Shiu, J.-H. Lin, D.-H. Wei, H.-J. Lin, Y.-J. Hsu, *ACS Appl. Nano Mater* **2021**, *4*, 5240.
[4] I. J. McDonald, M. E. Jamer, K. L. Krycka, E. Anber, D. Foley, A. C. Lang, W. D. Ratcliff, D. Heiman, M. L. Taheri, J. A. Borchers, L. H. Lewis, *ACS Appl. Nano Mater* **2019**, *2*, 1940.
[5] *Nanoscale Magnetic Materials and Applications* (Eds: J. P. Liu, E. Fullerton, O. Gutfleisch, D. J. Sellmyer), Springer US, Boston, MA **2009**.
[6] B. Balasubramanian, B. Das, R. Skomski, W. Y. Zhang, D. J. Sellmyer, *Adv. Mater.* **2013**, *25*, 6090.
[7] E. F. Kneller, R. Hawig, *IEEE Trans. Magn.* **1991**, *27*, 3588.
[8] J. S. Jiang, S. D. Bader, *J. Phys. Condens. Matter* **2014**, *26*, 064214.
[9] G. Varvaro, A. Omelyanchik, D. Peddis, *Tailored Functional Oxide Nanomaterials*, Wiley, Hoboken, New Jersey **2022**.
[10] C. De Julian Fernandez, C. Sangregorio, J. De La Figuera, B. Belec, D. Makovec, A. Quesada, *J. Phys. D. Appl. Phys* **2020**, *54*, 53001.
[11] B. Muzzi, M. Albino, C. Innocenti, M. Petrecca, B. Cortigiani, C. D. J. Fernández, G. Bertoni, R. Fernandez-Pacheco, A. Ibarra, C. Marquina, M. R. Ibarra, C. Sangregorio, *Nanoscale* **2020**, *12*, 14076.
[12] E. E. Fullerton, J. Jiang, S. Bader, *J. Magn. Magn. Mater.* **1999**, *200*, 392.
[13] F. Sayed, G. Kotnana, G. Muscas, F. Locardi, A. Comite, G. Varvaro, D. Peddis, G. Barucca, R. Mathieu, T. Sarkar, *Nanoscale Adv* **2020**, *2*, 851.
[14] B. Balamurugan, D. J. Sellmyer, G. C. Hadjipanayis, R. Skomski, *Scr. Mater.* **2012**, *67*, 542.
[15] R. Skomski, P. Manchanda, P. K. Kumar, B. Balamurugan, A. Kashyap, D. J. Sellmyer, *IEEE Trans. Magn.* **2013**, *49*, 3215.
[16] J. Cui, M. Kramer, L. Zhou, F. Liu, A. Gabay, G. Hadjipanayis, B. Balasubramanian, D. Sellmyer, *Acta Mater.* **2018**, *158*, 118.
[17] N. Jones, *Nature* **2011**, *472*, 22.
[18] H. Zeng, J. Li, J. P. Liu, Z. L. Wang, S. Sun, *Nature* **2002**, *420*, 395.
[19] C. Granados-Miralles, M. Saura-Múzquiz, H. L. Andersen, A. Quesada, J. V. Ahlburg, A.-C. Dippel, E. Canévet, M. Christensen, *ACS Appl. Nano Mater* **2018**, *1*, 3693.
[20] D. Primc, D. Makovec, *Nanoscale* **2015**, *7*, 2688.
[21] B. Belec, G. Dražić, S. Gyergyek, B. Podmiljšak, T. Goršak, M. Komelj, J. Nogués, D. Makovec, *Nanoscale* **2017**, *9*, 17551.

[22] A. Omelyanchik, S. Villa, M. Vasilakaki, G. Singh, A. M. Ferretti, A. Ponti, F. Canepa, G. Margaris, K. N. Trohidou, D. Peddis, *Nanoscale Adv* **2021**, *3*, 6912.
[23] A. López-Ortega, M. Estrader, G. Salazar-Alvarez, A. G. Roca, J. Nogués, *Phys. Rep.* **2015**, *553*, 1.
[24] X. Liu, S. Zuo, H. Wang, T. Zhang, Y. Dong, C. Jiang, *RSC Adv.* **2022**, *12*, 7568.
[25] M. Casavola, A. Falqui, M. A. Garci?A, M. Garci?A-Herna?Ndez, C. Giannini, R. Cingolani, P. D. Cozzoli, *Nano Lett.* **2009**, *9*, 366.
[26] E. A. Gorbachev, L. A. Trusov, A. D. Kovalenko, A. V. Morozov, P. E. Kazin, *Nanoscale* **2021**, *13*, 18340.
[27] P. Jenus, M. Topole, P. Mcguiness, C. Granados-Miralles, M. Stingaciu, M. Christensen, S. Kobe, K. Zuzek Rozman, *J. Am. Ceram. Soc.* **2016**, *99*, 1927.
[28] D. Roy, P. S. Anil Kumar, *AIP Adv.* **2015**, *5*, 077137.
[29] P. Maltoni, T. Sarkar, G. Barucca, G. Varvaro, F. Locardi, D. Peddis, R. Mathieu, *J. Phys. Chem. C* **2021**, *125*, 5927.
[30] F. H. Gjørup, M. Saura-Múzquiz, J. V. Ahlburg, H. L. Andersen, M. Christensen, *Materialia* **2018**, *4*, 203.
[31] J. M. D. Coey, *Magnetism and Magnetic Materials*, Cambridge University Press, Cambridge, MA **2001**.
[32] A. F. Manchón-Gordón, P. E. Sánchez-Jiménez, J. S. Blázquez, A. Perejón, L. A. Pérez-Maqueda, *J. Alloys Compd.* **2022**, *922*, 166203.
[33] G. D. Soria, P. Jenus, J. F. Marco, A. Mandziak, M. Sanchez-Arenillas, F. Moutinho, J. E. Prieto, P. Prieto, J. Cerdá, C. Tejera-Centeno, S. Gallego, M. Foerster, L. Aballe, M. Valvidares, H. B. Vasili, E. Pereiro, A. Quesada, J. de la Figuera, *Sci. Rep.* **2019**, *9*, 11777.
[34] G. Muscas, P. Anil Kumar, G. Barucca, G. Concas, G. Varvaro, R. Mathieu, D. Peddis, *Nanoscale* **2016**, *8*, 2081.
[35] P. Shyam, M. Mørch, A. Z. Eikeland, J. Ahlburg, A. Mamakhel, M. Saura-Múzquiz, M. Christensen, *Mater. Chem. Front.* **2022**, *6*, 2422.
[36] E. H. Sánchez, M. Vasilakaki, S. S. Lee, P. S. Normile, G. Muscas, M. Murgia, M. S. Andersson, G. Singh, R. Mathieu, P. Nordblad, P. C. Ricci, D. Peddis, K. N. Trohidou, J. Nogués, J. A. De Toro, *Chem. Mater.* **2020**, *32*, 969.
[37] R. Antón, J. González, J. Andrés, P. Normile, J. Canales-Vázquez, P. Muñiz, J. Riveiro, J. De Toro, *Nanomaterials* **2017**, *7*, 61.
[38] J. P. Liu, R. Skomski, Y. Liu, D. J. Sellmyer, *J. Appl. Phys.* **2000**, *87*, 6740.
[39] A. Quesada, C. Granados-Miralles, A. López-Ortega, S. Erokhin, E. Lottini, J. Pedrosa, A. Bollero, A. M. Aragón, F. Rubio-Marcos, M. Stingaciu, G. Bertoni, C. De Julián Fernández, C. Sangregorio, J. F. Fernández, D. Berkov, M. Christensen, *Adv. Electron. Mater.* **2016**, *2*, 1500365.
[40] P. Maltoni, T. Sarkar, G. Varvaro, G. Barucca, S. A. Ivanov, D. Peddis, R. Mathieu, *J. Phys. D. Appl. Phys.* **2021**, *54*, 124004.
[41] C. N. Chinnasamy, B. Jeyadevan, K. Shinoda, K. Tohji, D. J. Djayaprawira, M. Takahashi, R. J. Joseyphus, A. Narayanasamy, *Appl. Phys. Lett.* **2003**, *83*, 2862.
[42] L. Zhao, H. Zhang, Y. Xing, S. Song, S. Yu, W. Shi, X. Guo, J. Yang, Y. Lei, F. Cao, *J. Solid State Chem.* **2008**, *181*, 245.
[43] C. Carvallo, A. R. Muxworthy, D. J. Dunlop, *Phys. Earth Planet. Inter.* **2006**, *154*, 308.
[44] A. P. Roberts, D. Heslop, X. Zhao, C. R. Pike, *Rev. Geophys.* **2014**, *52*, 557.
[45] M. R. Zamani Kouhpanji, A. Ghoreyshi, P. B. Visscher, B. J. H. Stadler, *Sci. Rep.* **2020**, *10*, 15482.
[46] P. Rani, G. Muscas, H. Stopfel, G. Andersson, P. E. Jönsson, *Adv. Electron. Mater.* **2020**, *6*, 2000573.
[47] D. A. Gilbert, J. W. Liao, B. J. Kirby, M. Winklhofer, C. H. Lai, K. Liu, *Sci. Rep.* **2016**, *6*, 32842.
[48] J. A. De Toro, M. Vasilakaki, S. S. Lee, M. S. Andersson, P. S. Normile, N. Yaacoub, P. Murray, E. H. Sánchez, P. Muñiz, D. Peddis, R. Mathieu, K. Liu, J. Geshev, K. N. Trohidou, J. Nogués, *Chem. Mater.* **2017**, *29*, 8258.
[49] F. Béron, L. A. S. De Oliveira, M. Knobel, K. R. Pirota, *J. Phys. D. Appl. Phys.* **2013**, *46*, 045003.
[50] E. Goto, N. Hayashi, T. Miyashita, K. Nakagawa, *J. Appl. Phys.* **1965**, *36*, 2951.
[51] P. Maltoni, G. Varvaro, M. Abdolrahimi, D. Peddis, R. Mathieu, *J. Appl. Phys.* **2023**, *133*.
[52] P. Maltoni, S. A. Ivanov, G. Barucca, G. Varvaro, D. Peddis, R. Mathieu, *Sci. Rep.* **2021**, *11*, 23307.
[53] D. Peddis, P. E. Jönsson, S. Laureti, G. Varvaro, *Front. Nanosci.* **2014**, *6*, 129.
[54] G. C. Lavorato, D. Peddis, E. Lima, H. E. Troiani, E. Agostinelli, D. Fiorani, R. D. Zysler, E. L. Winkler, *J. Phys. Chem. C* **2015**, *119*, 15755.
[55] V. Patel, M. El-Hilo, K. O'grady, R. W. Chantrell, *J. Phys. D. Appl. Phys.* **1993**, *26*, 1453.
[56] J. D. Dutson, K. O'grady, Bin Lu, Y. Kubota, C. L. Platt, *IEEE Trans. Magn.* **2003**, *39*, 2344.
[57] T. Deakin, K. O'grady, *J. Appl. Phys.* **2008**, *103*, 07F503.
[58] M. El-Hilo, K. O'grady, R. W. Chantrell, *J. Magn. Magn. Mater.* **1993**, *120*, 244.
[59] J. Chureemart, L. Lari, T. P. Nolan, K. O'grady, *J. Appl. Phys.* **2013**, *114*, 083907.
[60] G. D. Soria, J. F. Marco, A. Mandziak, S. Sánchez-Cortés, M. Sánchez-Arenillas, J. E. Prieto, J. Dávalos, M. Foerster, L. Aballe, J. López-Sánchez, J. C. Guzmán-Mínguez, C. Granados-Miralles, J. De La Figuera, A. Quesada, *J. Phys. D. Appl. Phys.* **2020**, *53*, 344002.
[61] J. C. Slonczewski, *Phys. Rev.* **1958**, *110*, 1341.
[62] M. Petrecca, B. Muzzi, S. M. Oliveri, M. Albino, N. Yaacoub, D. Peddis, C. De Julián Fernández, C. Innocenti, C. Sangregorio, *J. Phys. D. Appl. Phys.* **2021**, *54*, 134003.
[63] S. Bernal, F. Botana, J. Calvino, C. López-Cartes, J. Pérez-Omil, J. Rodrıǵuez-Izquierdo, *Ultramicroscopy* **1998**, *72*, 135.
[64] J. Rodríguez-Carvajal, *Phys. B Condens. Matter* **1993**, *192*, 55.
[65] M. Saura-Múzquiz, C. Granados-Miralles, M. Stingaciu, E. D. Bøjesen, Q. Li, J. Song, M. Dong, E. Eikeland, M. Christensen, *Nanoscale* **2016**, *8*, 2857.
[66] J. I. Langford, A. J. C. Wilson, *J. Appl. Crystallogr.* **1978**, *11*, 102.
[67] C. R. Pike, A. P. Roberts, K. L. Verosub, *J. Appl. Phys.* **1999**, *85*, 6660.
[68] K. O'Grady, H. Laidler, *J. Magn. Magn. Mater.* **1999**, *200*, 616.
[69] R. J. Harrison, J. M. Feinberg, *Geochem. Geophys. Geosyst.* **2008**, *9*, Q05016.
[70] I. D. Mayergoyz *Mathematical Models of Hysteresis*, Springer, New York, NY **1991**.